Electronic Supplemental Information for:

Indoor aerosol water content and phase state in U.S. residences: Impacts of relative humidity, aerosol mass and composition, and mechanical system operation

Bryan E. Cummings[1], Ying Li[2], Peter F. DeCarlo[3], Manabu Shiraiwa[2], Michael S. Waring[1,*]

[1]Drexel University, Philadelphia, Pennsylvania, USA
[2]University of California, Irvine, California, USA
[3]Johns Hopkins University, Baltimore, Maryland, USA

[*]*Corresponding email: msw59@drexel.edu*

Contents

1. 2D-VBS information

Description of VBS space

The 2D-VBS is a tool that allows all organic matter (OM), that is material in either the gas or particle phases, to be organized by volatility and oxygenation. The *x*-axis represents volatility, parameterized by the effective saturation concentration (C^*, µg/m^3). Oxygenation is represented on the *y*-axis, parameterized by the ratio of oxygen atoms to carbon atoms (O:C). The 2D-VBS discretizes C^* into 15 log-spaced bins spanning 10^{-5} to 10^9 µg/m^3, and O:C is discretized into 11 bins spaced at intervals of 0.1 between 0 and 1.0. This discretization yields 165 bins for OM to occupy.

Descriptions of where different types of molecules and OA factors generally reside within this are available in the literature.[1–3] OM may also migrate throughout this space due to oxidative reactions, known as OA aging. Descriptions of this type of movement have also been published.[4–6] Indoor OA aging was explored by Cummings and Waring (see below).[7] Although that study did not find aging to significantly impact OA under time-average simulations (as are run in the study employed within the accompanying main text), they are included as a permanent part of IMAGES intended for use in time-varying investigations, so it remains here for completeness.

Within IMAGES, the 2D-VBS is reshaped into a one-dimensional array for computational purposes, per the following example showing the transformation for the OM concentration array:

$$\begin{bmatrix} C_1 & \cdots & C_{15} \\ C_{16} & \cdots & C_{30} \\ \vdots & \ddots & \vdots \\ C_{151} & \cdots & C_{165} \end{bmatrix} \rightarrow \begin{bmatrix} C_1 & C_2 & \cdots & C_{165} \end{bmatrix} \equiv C \tag{S1.1}$$

This transformation algorithm also applies to parameters that may be constrained within the 2D-VBS space, including the C^* axis itself and the aerosol mass fraction (AMF, ξ), which facilitated the computation of the partitioning Equations 3-6 in the main text.

Mass balance equations for OM aging reactions

The array-like term, $\boldsymbol{A}_{\mathrm{OM}}$ (µg m^{-3} h^{-1}), present in Table 1 in the main text, describes the movement of OM about the 2D-VBS due to reactions between OH and saturated OM. A transformation matrix, T, describes that movement, and conserves mass of organic carbon (OC) by design, allowing O- and H-containing functional groups to be added or removed to molecules. Also, gas-phase reactions follow second order kinetics (with a reaction rate constant that may vary by VBS bin: $\boldsymbol{k}_{\mathrm{g}}$, ppb^{-1} h^{-1}), while heterogeneous reactions, not strictly being second order reactions, occur more slowly due to uptake and diffusion limitation. These are described with an "effective" second order reaction rate constant (k_{het}, ppb^{-1} h^{-1}), estimated to be ten times slower than k_{g}. The resulting expression is:

$$A_{OM} = C_{OH}\left[k_g\Gamma\left(C_{OC}(1-\xi) \times (T-I)\right) + k_{het}\Gamma\left(C_{OC}\xi \times (T-I)\right)\right] \quad \text{S1.2}$$

where C_{OH} (ppb) is the OH concentration; the conversion factor $\boldsymbol{\Gamma}$ in this equation is the OM/OC ratio as an array for all VBS bins; $\boldsymbol{C}_{OC}$ (μg/m^3) is the concentration array of OC only; $\mathbf{I}$ is the identity matrix; and " × " denotes matrix multiplication. This term is derived in Cummings and Waring[7] for use in this indoor model, and is based on the works of Donahue et al.[4] The expression used for $\boldsymbol{k}_g$ is in Donahue et al.[8]

OH recycling was neglected from this work, so all OM aging reactions acted as a sink for OH. This was accounted for in Table 1 in the main text with the scalar value A_{OH} (h^{-1}):

$$A_{OH} = \left(k_g \cdot (\Gamma C_{OM}(1-\xi))\right) + \left(k_{het} \cdot (\Gamma C_{OM}\xi)\right) \quad \text{S1.3}$$

where the conversion factor $\boldsymbol{\Gamma}$ in this equation serves to convert $\boldsymbol{C}_{OM}$ from units of μg/m^3 to ppb, which will depend on air temperature; and " · " denotes the dot product.

Constraining "average" OM parameters

Within the model, several OA parameters (e.g. density, hygroscopicity, and T_g) are characterized by O:C and/or C^*. Thus, determining the values of these parameters in each 2D-VBS bin is straightforward. However, their values as they relate to the OA particle as a whole must be constrained. The average C^* and O:C values of any OM distribution are the x- and y-coordinates, respectively, of the centroid of that distribution strewn across the 2D-VBS space. Because the density, hygroscopicity, and T_g parameters relate to the particle in particular, the centroid of the distribution representing only the particle-phase OM must be used in order to obtain appropriate O:C and C^* values.

This concept is visualized in Figure S1 as it relates to the 2D-VBS space. Figure S1.a shows the centroid for the total gas- and particle-phase steady state OM computed by an arbitrarily-selected run of the simulations set forth for the study presented in the main text. Figure S1.b shows the centroid for the particle phase OM after applying the partitioning equations

Within IMAGES, which only deals with one-dimensional arrays, the centroid C^* and O:C coordinates for the particle-phase OM (i.e. $C^*_{OA,avg}$, $[O{:}C]_{OA,avg}$) are the weighted averages of each over all 2D-VBS bins, where the weights correspond to the fractional amount of OM each bin contributes to the total OA concentration:

$$C^*_{OA,avg} = \frac{C^* \cdot (\xi C_{OM})}{\sum \xi C_{OM}} \quad \text{S1.4}$$

$$[O{:}C]_{OA,\,avg} = \frac{[\boldsymbol{O{:}C}] \cdot (\boldsymbol{\xi C_{OM}})}{\sum \boldsymbol{\xi C_{OM}}} \qquad \text{S1.5}$$

where the bolded terms indicate vectors so that [**O:C**] contains all of the O:C values corresponding to each bin in the 2D-VBS, indexed according to the transformation shown in Equation S.1; ***C**** contains all of the C^* values corresponding to each bin in the 2D-VBS; $\boldsymbol{\xi}$ contains the AMF in each bin, and C_{OM} contains the total OM concentrations in each bin. The " · " symbol indicates the dot product, whereas element-wise multiplication between arrays is otherwise applied.

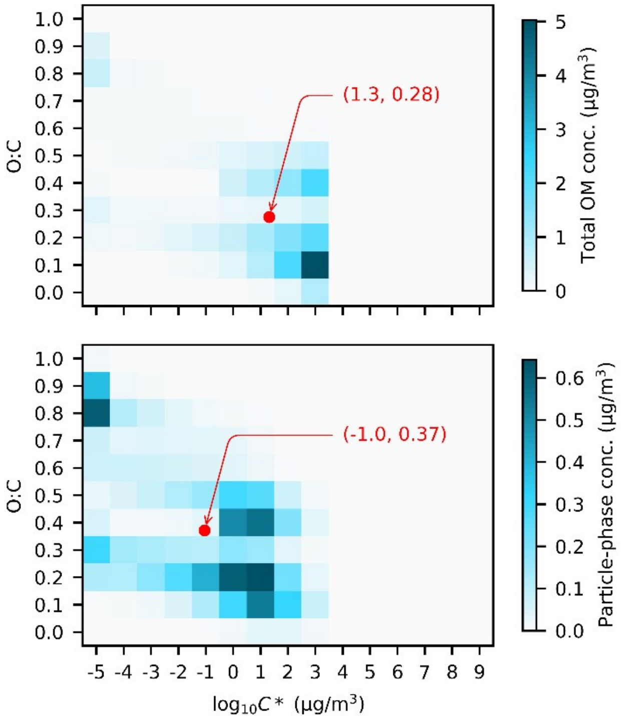

Figure S1. The total OM (a) and particle phase OM (b) distributions throughout the 2D-VBS space for one of the runs set forth as a part of the investigation presented in the main text. The centroids for each, corresponding to the average O:C and C* values, are marked by the red point.

O:C and volatility distribution definitions for OA factors

Table S1. Volatility distributions and average O:C values of all OA factors considered by this work.

Factor	avg. O:C	OM mass fraction in $\log_{10}C^*$ bin										
		-7	-6	-5	-4	-3	-2	-1	0	1	2	3
HOA[A,C]	0.128	0	0.015	0.016	0.018	0.021	0.028	0.041	0.067	0.121	0.228	0.445
COA[B,C]	0.195	0	0	0	0	0.06	0.01	0.01	0.04	0.73	0.15	0
SVOOA[A,C]	0.509	0	0	0.043	0.050	0.059	0.072	0.089	0.113	0.144	0.187	0.244
LVOOA[A,C]	0.810	0.315	0.217	0.150	0.104	0.071	0.050	0.034	0.024	0.016	0.012	0.008
SOA[D]	0.4	-	-	-	-	-	-	-	-	-	-	-

A: Volatility distribution from Cappa and Jimenez[9]

B: Volatility distribution from Takhar et al.[10]

C: Average O:C from Canagaratna et al.[11]

D: SOA mass yields for various VOC oxidation reactions were taken from Waring[12]

2. Derivation: Growth factor

From Equation 7 in the main text, κ-Köhler theory states that:

$$\frac{V_{AW}}{V_d} = \frac{\alpha_w}{(1 - \alpha_w)}\kappa \qquad \text{S2.1}$$

which relates the volume of the AW taken up by a particle at a certain water activity to that dry particle's volume in completely dry air. The growth factor (GF) instead defines the ratio of the mobility diameters between the wet (AW + dry material) and dry particle. To arrive at this relation, Equation S2.1 is altered so that the left-hand side (LHS) instead represents the ratio of the wet particle to dry particle volumes:

$$\frac{V_{AW}}{V_d} + \frac{V_d}{V_d} = \frac{\alpha_w}{(1 - \alpha_w)}\kappa + \frac{V_d}{V_d} \qquad \text{S2.2}$$

$$\frac{V_{AW} + V_d}{V_d} = \frac{\alpha_w}{(1 - \alpha_w)}\kappa + 1 \qquad \text{S2.3}$$

The numerator of the LHS can more succinctly be referred to as V_{wet}, the volume of the total wetted particle:

$$\frac{V_{wet}}{V_d} = \frac{\alpha_w}{(1 - \alpha_w)}\kappa + 1 \qquad \text{S2.4}$$

Because volume ratios are just the cube of diameter ratios:

$$\frac{d_{wet}}{d_d} = \left(\frac{\alpha_w}{(1 - \alpha_w)}\kappa + 1\right)^{1/3} \equiv GF \qquad \text{S2.5}$$

which is definition of the GF.

3. Accounting for temperature impacts on DRH

Table 2 in the main text provides DRH values from the literature that were measured at a reference temperature (T_0) of 298 K. The DRH for any salt *i* at any temperature (*T*, K) is determined by:

$$DRH_i = DRH_i^0 \exp\left[\frac{M_w S_i L_i}{M_i R}\left(\frac{1}{T_0} - \frac{1}{T}\right)\right] \tag{S3.1}$$

where DRH_i^0 is the salt's known DRH at 298 K; M_w and M_i are the molecular weights (g/mol) of water (M_w = 18 g/mol) and salt *i*, respectively; S_i is the solubility of the salt in water (grams of salt per grams of water, g/g); L_i (kJ/mol) is the latent heat of fusion for the salt from a saturated aqueous solution; and *R* (kJ mol^{-1} K^{-1}) is the universal gas constant. Each salt's reference DRH, *M*, *S*, and *L* values are presented in the below Table S2. Due to scarce information in the literature, potential temperature impacts on ERH values were neglected.

Table S2. Reference DRH values for simulated IA salts, and parameters required to adjust DRH based on temperature changes using Equation S3.1.

Component	DRH	*M* (g/mol)	*S*	*L* (kJ/mol)
Ammonium Nitrate	0.621	80.04	2.13	-15.16
Ammonium Sulfate	0.802	132.14	0.746	-6.35
Sodium Chloride	0.753	58.44	0.36	-1.853
Potassium Chloride	0.85	74.55	0.355	-17.22

4. Derivation: recirculated to non-recirculated mass ratio

Consider an indoor environment, with two distinct routes for pollutant removal:

i. L_p (h^{-1}) – which permanently and irreversibly removes a contaminant out of the system.

ii. L_r (h^{-1}) – which removes a contaminant from the room en route to the recirculation HVAC system, where it is conditioned and reintroduced to the room.

Now consider two populations of indoor PM represented by concentrations:

i. $C_{no\text{-}r}$ ($\mu g/m^3$) – which consists of PM which has been freshly introduced (not recirculated) into the indoor space, yet to be affected by either L_o or L_r mechanisms.

ii. C_r ($\mu g/m^3$) – which consists of PM which has previously been lost to L_r, conditioned, filtered, and reintroduced into the space.

Both PM populations are generated from mutually exclusive sources:

i. $S_{no\text{-}r}$ ($\mu g\ h^{-1}\ m^{-3}$) produces $C_{no\text{-}r}$

ii. S_r ($\mu g\ h^{-1}\ m^{-3}$) produces C_r.

Yet both $C_{no\text{-}r}$ and C_r are equally susceptible to both L_p and L_r mechanisms. From these constraints, two differential mass balance equations can be constructed for each PM population:

$$\frac{dC_{no-r}}{dt} = S_{no-r} - (L_p + L_r)C_{no-r} \tag{S4.1}$$

$$\frac{dC_r}{dt} = S_r - (L_p + L_r)C_r \tag{S4.2}$$

The steady state solutions to differential Equations S4.1 and S4.2, respectively, are:

$$C_{no-r} = \frac{S_{no-r}}{L_p + L_r} \tag{S4.3}$$

$$C_r = \frac{S_r}{L_p + L_r} \tag{S4.4}$$

$L_{no\text{-}r}$ may be due to ventilation air exchange (λ_v, h^{-1}) or surface deposition (β, h^{-1}), so:

$$L_p = \lambda_v + \beta \tag{S4.5}$$

(currently neglecting phase partitioning or chemical reactions). And L_r can only be due to recirculation air exchange (λ_r, h^{-1}) through the residential HVAC system:

$$L_r = \lambda_r \tag{S4.6}$$

The PM reentering the space from the HVAC system by S_r depends on the total PM concentration susceptible to L_r (i.e. $C_{no\text{-}r} + C_r$), L_r itself (i.e. λ_r), and the HVAC filter efficiency (η):

$$S_r = \lambda_r(1-\eta)\left(C_{no-r} + C_r\right) \tag{S4.7}$$

Appropriately substituting Equations S4.5-S4.7 into Equation S4.4 results in:

$$C_r = \frac{\lambda_r(1-\eta)\left(C_{no-r} + C_r\right)}{\lambda_v + \beta + \lambda_r} \tag{S4.8}$$

Rearranging the terms in Equation S4.8 as follows allows the steady state C_r to be explicitly solved for:

$$C_r\left(\lambda_v + \beta + \lambda_r\right) = \lambda_r(1-\eta)\left(C_{no-r} + C_r\right) \tag{S4.9}$$

$$C_r\left(\lambda_v + \beta + \lambda_r\right) = \lambda_r(1-\eta)C_{no-r} + \lambda_r(1-\eta)C_r \tag{S4.10}$$

$$C_r\left(\lambda_v + \beta + \lambda_r - \lambda_r(1-\eta)\right) = \lambda_r(1-\eta)C_{no-r} \tag{S4.11}$$

$$C_r = \frac{\lambda_r(1-\eta)C_{no-r}}{\lambda_v + \beta + \lambda_r - \lambda_r(1-\eta)} \tag{S4.12}$$

$$C_r = \frac{\lambda_r(1-\eta)C_{no-r}}{\lambda_v + \beta + \lambda_r - \lambda_r + \lambda_r\eta} \tag{S4.13}$$

$$C_r = \frac{\lambda_r(1-\eta)C_{no-r}}{\lambda_v + \beta + \lambda_r\eta} \tag{S4.14}$$

From Equation S4.14, the steady state ratio between C_r and $C_{no\text{-}r}$ can easily be obtained:

$$\frac{C_r}{C_{no-r}} = \frac{\lambda_r(1-\eta)}{\lambda_v + \beta + \lambda_r\eta} \tag{S4.15}$$

Note that this ratio is not dependent on the strength of the source, $S_{no\text{-}r}$, of $C_{no\text{-}r}$, which may include outdoor-to-indoor air exchange, indoor emissions, and other indoor sources. This ratio can be converted into a fraction of total concentration which is C_r, or the fraction of PM which has been recirculated and has traversed the HVAC (f_r), by diving through by $C_{no\text{-}r}$:

$$f_r = \frac{C_r}{C_r + C_{no-r}} = \frac{\left(\frac{C_r}{C_{no-r}}\right)}{\left(\frac{C_r}{C_{no-r}}\right) + 1} \quad \text{S4.16}$$

5. Computing select indoor model inputs

Surface deposition rate

Rackes and Waring[13] produced a second order polynomial expression for PM surface deposition (β_{PM}, h^{-1}) as a function of the HVAC filtration rate (η_{PM}):

$$\beta_{PM} = 0.171{\eta_{PM}}^2 - 0.1378\eta_{PM} + 0.0918 \qquad \text{S5.1}$$

This was shown to produce a good fit with an $R^2 = 0.983$. This empirical relationship was used to constrain β_{PM} in the model after η_{PM} was sampled from its input distribution.

HVAC runtime

The fractional runtime of the residential HVAC recirculation system (f_{RT}) was derived from the work of Touchie and Seigel[14]. They measured f_{RT} for ~7000 homes in North America and plotted them against the outdoor temperature (T_{out}, °C). They also provided linear equations of best fit for both cooling and heating conditions:

$$f_{RT,heat} =- 0.0068T_{out} + 0.207 \qquad \text{S5.2}$$

$$f_{RT,cool} = 0.0112T_{out} + 0.0277 \qquad \text{S5.3}$$

In this work, heating was enforced anytime $T_{\mathrm{out}} < 15$ °C, and cooling was enforced anytime $T_{\mathrm{out}} > 21$ °C. Although Touchie and Seigel[14] often observed recirculation systems operating at low frequencies within this deadband zone, for simplicity in our work, no recirculation was assumed (i.e. $f_{\mathrm{RT}} = 0$) if T_{out} was between the enforced deadband.

Indoor RH

Nguyen et al.[15] found this relationship between outdoor and indoor absolute humidity (AH, g/m^3):

$$AH_{in} = 0.69AH_{out} + 3.2 \qquad \text{S5.4}$$

to best describe their observations of homes in Boston ($R^2 = 0.83$). By visual inspection, this parameterization also fit the trends observed by Nguyen and Dockery[16] for multiple cities reasonably well. For homes in hot and humid cities that employed air conditioning, Figure 3 in Nguyen and Dockery[16] showed that increases in $\mathrm{AH_{in}}$ with increasing $\mathrm{AH_{out}}$ were diminished at higher AH values, deviating from the relation of Equation S5.4. This occurrence was attributed to loss of water vapor via condensation over cooling coils.

Our procedure for constraining the indoor RH was informed by this set of observation, and is as follows:

1. RH_{out} was appropriately converted to AH considering T_{out}.
2. This AH_{out} was fed to Equation S5.4 to obtain a first-estimate of AH_{in}.
3. Statistical variation was simulated by sampling a residual to be applied to the AH_{in} predicted by Step 2 from a normal distribution.
4. If cooling is being provided, the additional loss rate of water (g m^{-3} h^{-1}) from the airstream would be proportional to the recirculation AER (λ_r, h^{-1}), f_{RT}, and the AH, and so the AH_{in} predicted by Step 3 would be reduced proportionally to this loss rate.
5. The final AH_{in} was appropriately converted to RH considering T_{in}.
6. Since this approach is statistical, not physical, some RH_{in} may be greater than 100%. Any RH_{in} values above 95% were reduced to 95%.

This procedure, as it relates to AH, is encapsulated by the following Equation:

$$AH_{in} = 0.69AH_{out} + 3.2 + N(0, \sigma) + \alpha f_{RT,cool}\lambda_r AH_{out} \qquad \text{S5.5}$$

Where:

- The first two terms account for the Nguyen et al.[15] relationship from Equation S5.4, the third terms accounts for statistical variability, and the fourth term accounts for coil loss proportional to a constant, α, and the flow rate of water over the coil (using AH_{out} rather than AH_{in} in this fourth term simplifies the required math and provides a good enough water loss proxy for our purposes).
- $N(0, \sigma)$ represents a random sample from a normal distribution defined with a mean of zero and standard deviation of σ. To avoid negative numbers and extreme outliers, only samples within the 95% confidence interval of this distribution were allowed.
- When $T_{out} > 21$ °C, $f_{RT,cool}$ is governed by Equation S5.3; and $f_{RT,cool} = 0$ any time $T_{out} \leq 21$ °C.
- Per engineering judgement, we deemed $\sigma = 0.5$, and $\alpha = -0.06$

The progression of this procedure is shown in Figure S2 as it relates to all 9938 of our model instances. All AH_{out} values used in our simulations are scattered against:

i. (Figure S2.a) the AH_{in} predicted by the simple linear Equation S5.4.
ii. (Figure S2.b) the AH_{in} values adjusted by Step 3.
iii. (Figure S2.c) all final AH_{in} values used to obtain RH_{in} including water loss adjustments by Step 4 as appropriate.

The AH_{in} values appropriately converted to RH_{in} according to T_{out} are shown in Figure S3 as a histogram. Of the 9938 instances, this procedure only yielded 18 that initially produced $\text{RH}_{\text{in}} > 100\%$. However, for additional stability of our results, we truncated the maximum allowed RH_{in} for IMAGES to consider to be 95%. Ultimately, this methodology produced 35 such cases that required truncation.

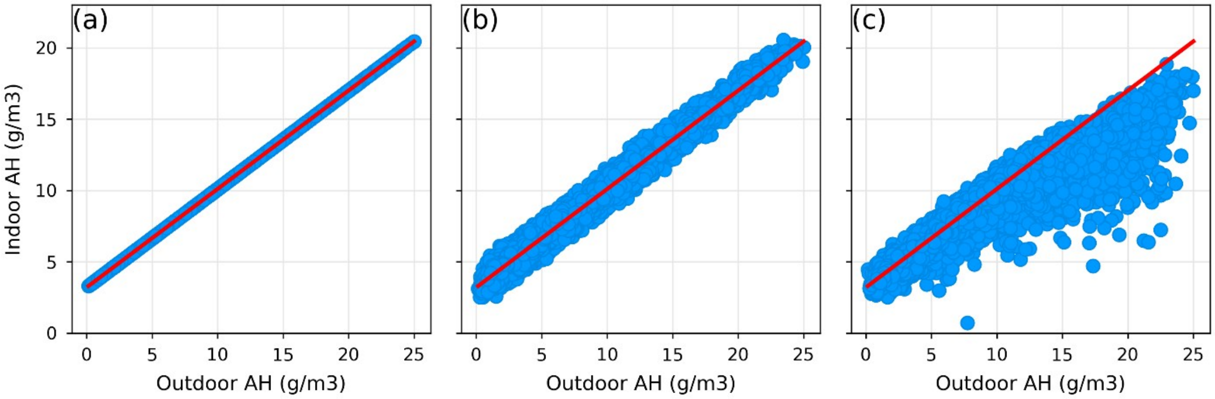

Figure S2. AH_{in}-AH_{out} scatter plots over all 9938 model instances showing the AH_{in} predicted by: **(a)** the Equation S5.4 from Nguyen et al.[15]; **(b)** the Equation S5.4 prediction including random variability; and **(c)** the final prediction including random variability and water loss to an operational cooling coil. The red line overlaid on each plot is the line produced by Equation S5.4, shown for reference. The points in pane **(c)** match in decent accordance with the observations made by Nguyen and Dockery[16] that were presented in their Figure 3.

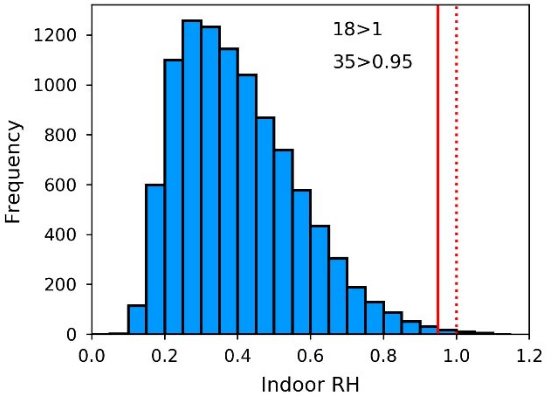

Figure S3. A histogram of the RH_{in} values converted from the AH_{in} values shown in Figure S2c. RH = 100% is marked with the dotted red line, and RH = 95% is marked with the solid red line. RH_{in} can never actually reach values greater than 100%, and this method only produced 18 of 9938 instances where this occurred. For further stability, we truncated the maximum possibile RH_{in} that IMAGES considered in these simulations to be 95%, which the methodology produced in 35 of the 9938 instances.

6. Speciated concentration summary table

Table S3. Summarized ranges of speciated PM concentrations.

Specie	Percentile (**In** Out)									
(µg/m^3)	1st		25th		Median		75th		99th	
Organics										
HOA	**0.014**	0.029	**0.297**	0.416	**0.654**	0.834	**1.27**	1.68	**5.44**	8.03
SVOOA	**0.076**	0.167	**0.374**	0.582	**0.631**	0.859	**0.987**	1.29	**2.59**	3.61
LVOOA	**0.073**	0.170	**0.357**	0.591	**0.594**	0.873	**0.936**	1.31	**2.70**	3.67
COA	**0.926**	-	**3.89**	-	**7.12**	-	**12.7**	-	**48.1**	-
SOA	**0.051**	-	**0.493**	-	**1.24**	-	**3.03**	-	**22.5**	-
OA$_{(org)}$	**2.40**	0.678	**7.15**	1.89	**11.6**	2.83	**19.2**	4.26	**65.0**	12.7
OA$_{(org+w)}$	**2.52**	0.797	**7.61**	2.22	**12.4**	3.38	**20.5**	5.15	**68.6**	16.2
AW$_{OA}$	**0.063**	0.020	**0.272**	0.192	**0.542**	0.439	**1.13**	0.853	**8.55**	4.73
Inorganics										
AN	**0.010**	0.052	**0.079**	0.341	**0.160**	0.622	**0.355**	1.46	**2.64**	10.9
AS	**0.073**	0.132	**0.443**	0.702	**0.814**	1.25	**1.49**	2.19	**5.23**	7.04
SC	**0**	0	**0**	0	**0**	0	**0**	0	**0.715**	0.986
PC	**0**	0	**0**	0	**0**	0	**0**	0	**0.391**	0.539
EC	**0.009**	0.016	**0.138**	0.228	**0.281**	0.422	**0.541**	0.762	**2.21**	2.84
GM	**0.017**	0.031	**0.154**	0.241	**0.312**	0.460	**0.650**	0.961	**4.26**	6.58
PIA	**0.272**	-	**1.09**	-	**1.92**	-	**3.36**	-	**13.0**	-
IA$_{(dry)}$	**1.06**	0.451	**3.12**	2.45	**4.55**	3.83	**6.58**	5.73	**16.6**	17.8
IA$_{(dry+w)}$	**1.16**	0.614	**3.41**	3.34	**5.13**	5.42	**7.64**	8.99	**22.7**	40.9
AW$_{IA}$	**0**	0	**0**	0.384	**0.329**	1.43	**0.994**	3.35	**8.88**	26.5
Total PM										
PM$_{(dry)}$	**4.31**	1.41	**11.2**	4.69	**16.7**	6.87	**25.6**	9.98	**74.6**	27.0
PM$_{(dry+w)}$	**4.62**	1.79	**12.1**	6.08	**18.2**	9.15	**28.1**	14.1	**83.1**	51.7
AW$_{PM}$	**0.059**	0.021	**0.359**	0.632	**0.949**	1.94	**2.15**	4.20	**16.8**	29.4

7. Validation of assuming organic-inorganic phase-separated particles

Bertram et al.[17] provided a simplified correlation for approximating RH_{LLPS}:

$$RH_{LLPS} = 0.355 + 3.399(O{:}C) - 4.718(O{:}C)^2 \tag{S7.1}$$

By applying this to all indoor OA results, it was determined that the median RH_{LLPS} = 87.8%, much higher than the median RH_{in} = 33.1%. Only 38 of the total 9938 (0.38%) total model instantiations produced an $RH_{in} > RH_{LLPS}$. Therefore, it was deemed appropriate to enforce IA and OA phase separation assumptions in all simulations.

8. Glass transition temperature vs. RH: Influence of O:C and *C**

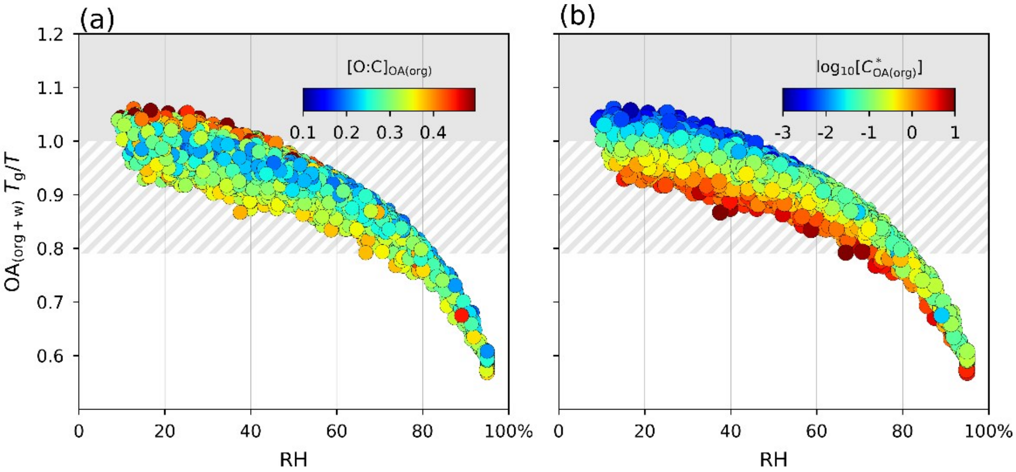

Figure S4. Showing the same T_g and RH points that are colored by OA concentration in Figure 5b in the main text, these scattered points are instead colored by the average O:C **(a)** and C^* **(b)** of OA. Because volatility is the main driver of $T_{g,OA(org)}$ (per Equation 14 in the main text), the $OA_{(org+w)}$ T_g/T consistently increases with decreasing C^*. $OA_{(org+w)}$ T_g/T generally increases with increasing O:C because low volatile organics tend to be highly oxidized, but a greater O:C may also lead to more uptake of water, lowering the $OA_{(org+w)}$ T_g/T.

9. Seasonal and regional trends in ambient and indoor IA and OA composition

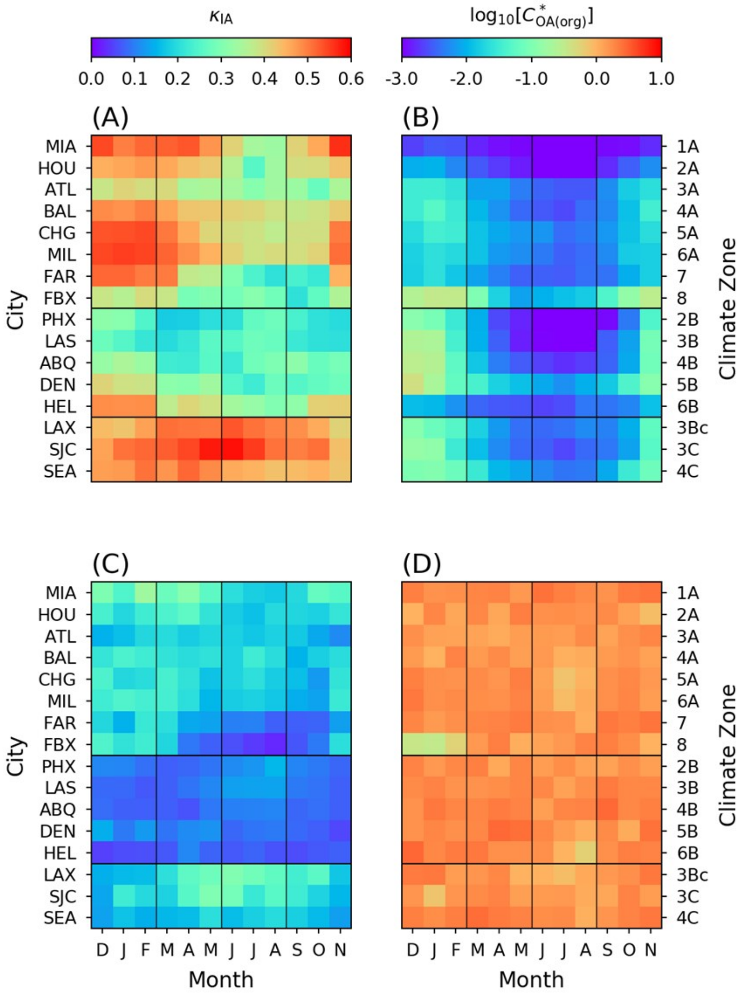

Figure S5. Not shown in the main text, this figure demonstrates the seasonal and regional variability in IA and OA composition, using κ_{IA} **(left column)** and OA C^* **(right column)**, respectively, as proxies. Both outdoor **(top row)** and outdoor **(bottom row)** heatmaps are provided for each. Considerable hygroscopicity variability exists outdoors, providing an explanation for some of the additional variability not caused by RH_{out} seen in the ambient AW and phase state heatmaps shown in Figure 6 in the main text. However, when mixed with dominant emitted aerosol indoors, the overall PM mix becomes more homogeneous in all climates, meaning that most indoor AW and phase state variability is due solely to RH_{in} variations.

10. T_g/T of phase separated OA populations

In the figure below, we provide estimates of how the phase states of the day-averaged OA predicted by the results presented in the main text might respond to scenarios where outdoor-sourced OA and indoor-emitted COA and SOA constitute three externally mixed populations, rather than forming a single OA phase. These estimates were generated by isolating the OM owing to each population predicted by the model runs described in the main text, and then partitioning each only into its own OA mass, considering neither a single absorbing OA mass nor gas-phase OM interaction between populations. This approach is simply a post-process method of approximating a physical condition that was not explicitly modeled. However, it is sufficient for exploring the question at hand.

These phase separated $OA_{(org+w)}$ T_g/T boxplots in the figure can be compared to baseline phase states of the internally mixed baseline aerosol. A concentration weighted average of the three populations would roughly produce the mixed OA baseline observed in our results. Still, the distinct COA and outdoor-sourced OA populations were predicted as a solid phase more often than if they were in a mixed aerosol because fewer higher-volatility organics can partition into smaller distinct OA masses, thereby increasing their $T_{g,OA(org)}$. While only ~25% of the baseline mixed OA particles were predicted to be solid, about half and ~70% of the distinct COA and outdoor-sourced OA, respectively, would be in a solid phase state. The distinct SOA phase state was more varied. It was frequently modeled to be liquid due to the relatively high volatility of its dominant organic constituents, while it may also be glassy at other times due to the small concentrations of nucleated SOA. This assessment must be validated by developing a robust kinetic model and validating it against observations.

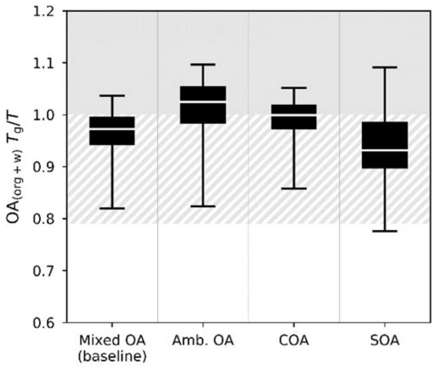

Figure S6. Boxplots showing approximations of the T_g/T ranges of potentially externally mixed OA populations, owing to outdoor-sourced OA, COA emitted from cooking activities, and nucleated SOA. The baseline T_g/T values of the internally mixed OA presented in the Results section are also shown for reference. The shown boxplot whiskers span the 95% confidence intervals. The hatched portion of the plot indicates where semisolid OA likely exists, below which (unshaded portion) OA is likely liquid, and above which (shaded portion) OA will be an amorphous solid.

References

(1) Jimenez, J. L.; Canagaratna, M. R.; Donahue, N. M.; Prevot, A. S. H.; Zhang, Q.; Kroll, J. H.; DeCarlo, P. F.; Allan, J. D.; Coe, H.; Ng, N. L.; Aiken, A. C.; Docherty, K. S.; Ulbrich, I. M.; Grieshop, A. P.; Robinson, A. L.; Duplissy, J.; Smith, J. D.; Wilson, K. R.; Lanz, V. A.; Hueglin, C.; Sun, Y. L.; Tian, J.; Laaksonen, A.; Raatikainen, T.; Rautiainen, J.; Vaattovaara, P.; Ehn, M.; Kulmala, M.; Tomlinson, J. M.; Collins, D. R.; Cubison, M. J.; E; Dunlea, J.; Huffman, J. A.; Onasch, T. B.; Alfarra, M. R.; Williams, P. I.; Bower, K.; Kondo, Y.; Schneider, J.; Drewnick, F.; Borrmann, S.; Weimer, S.; Demerjian, K.; Salcedo, D.; Cottrell, L.; Griffin, R.; Takami, A.; Miyoshi, T.; Hatakeyama, S.; Shimono, A.; Sun, J. Y.; Zhang, Y. M.; Dzepina, K.; Kimmel, J. R.; Sueper, D.; Jayne, J. T.; Herndon, S. C.; Trimborn, A. M.; Williams, L. R.; Wood, E. C.; Middlebrook, A. M.; Kolb, C. E.; Baltensperger, U.; Worsnop, D. R. Evolution of Organic Aerosols in the Atmosphere. *Science* **2009**, *326* (5959), 1525–1529. https://doi.org/10.1126/science.1180353.

(2) Donahue, N. M.; Epstein, S. A.; Pandis, S. N.; Robinson, A. L. A Two-Dimensional Volatility Basis Set: 1. Organic-Aerosol Mixing Thermodynamics. *Atmospheric Chemistry and Physics* **2011**, *11* (7), 3303–3318. https://doi.org/10.5194/acp-11-3303-2011.

(3) Donahue, N. M.; Kroll, J. H.; Pandis, S. N.; Robinson, A. L. A Two-Dimensional Volatility Basis Set – Part 2: Diagnostics of Organic-Aerosol Evolution. *Atmospheric Chemistry and Physics* **2012**, *12* (2), 615–634. https://doi.org/10.5194/acp-12-615-2012.

(4) Donahue, N. M.; Henry, K. M.; Mentel, T. F.; Kiendler-Scharr, A.; Spindler, C.; Bohn, B.; Brauers, T.; Dorn, H. P.; Fuchs, H.; Tillmann, R.; Wahner, A.; Saathoff, H.; Naumann, K.-H.; Möhler, O.; Leisner, T.; Müller, L.; Reinnig, M.-C.; Hoffmann, T.; Salo, K.; Hallquist, M.; Frosch, M.; Bilde, M.; Tritscher, T.; Barmet, P.; Praplan, A. P.; DeCarlo, P. F.; Dommen, J.; Prévôt, A. S. H.; Baltensperger, U. Aging of Biogenic Secondary Organic Aerosol via Gas-Phase OH Radical Reactions. *PNAS* **2012**, *109* (34), 13503–13508. https://doi.org/10.1073/pnas.1115186109.

(5) Chuang, W. K.; Donahue, N. M. A Two-Dimensional Volatility Basis Set – Part 3: Prognostic Modeling and NO_x Dependence. *Atmospheric Chemistry and Physics* **2016**, *16* (1), 123–134. https://doi.org/10.5194/acp-16-123-2016.

(6) Murphy, B. N.; Donahue, N. M.; Fountoukis, C.; Dall'Osto, M.; O'Dowd, C.; Kiendler-Scharr, A.; Pandis, S. N. Functionalization and Fragmentation during Ambient Organic Aerosol Aging: Application of the 2-D Volatility Basis Set to Field Studies. *Atmospheric Chemistry and Physics* **2012**, *12* (22), 10797–10816. https://doi.org/10.5194/acp-12-10797-2012.

(7) Cummings, B. E.; Waring, M. S. Predicting the Importance of Oxidative Aging on Indoor Organic Aerosol Concentrations Using the Two-Dimensional Volatility Basis Set (2D-VBS). *Indoor Air* **2019**, *29* (4), 616–629. https://doi.org/10.1111/ina.12552.

(8) Donahue, N. M.; Chuang, W.; Epstein, S. A.; Kroll, J. H.; Worsnop, D. R.; Robinson, A. L.; Adams, P. J.; Pandis, S. N. Why Do Organic Aerosols Exist? Understanding Aerosol Lifetimes Using the Two-Dimensional Volatility Basis Set. *Environ. Chem.* **2013**, *10* (3), 151–157. https://doi.org/10.1071/EN13022.

(9) Cappa, C. D.; Jimenez, J. L. Quantitative Estimates of the Volatility of Ambient Organic Aerosol. *Atmospheric Chemistry and Physics* **2010**, *10* (12), 5409–5424. https://doi.org/10.5194/acp-10-5409-2010.

(10) Takhar, M.; Stroud, C. A.; Chan, A. W. H. Volatility Distribution and Evaporation Rates of Organic Aerosol from Cooking Oils and Their Evolution upon Heterogeneous Oxidation. *ACS Earth Space Chem.* **2019**, *3* (9), 1717–1728. https://doi.org/10.1021/acsearthspacechem.9b00110.

(11) Canagaratna, M. R.; Jimenez, J. L.; Kroll, J. H.; Chen, Q.; Kessler, S. H.; Massoli, P.; Hildebrandt Ruiz, L.; Fortner, E.; Williams, L. R.; Wilson, K. R.; Surratt, J. D.; Donahue, N. M.; Jayne, J. T.; Worsnop, D. R. Elemental Ratio Measurements of Organic Compounds Using Aerosol Mass Spectrometry: Characterization, Improved Calibration, and Implications. *Atmospheric Chemistry and Physics* **2015**, *15* (1), 253–272. https://doi.org/10.5194/acp-15-253-2015.

(12) Wang, C.; Waring, M. S. Secondary Organic Aerosol Formation Initiated from Reactions between Ozone and Surface-Sorbed Squalene. *Atmospheric Environment* **2014**, *84*, 222–229. https://doi.org/10.1016/j.atmosenv.2013.11.009.

(13) Rackes, A.; Waring, M. S. Modeling Impacts of Dynamic Ventilation Strategies on Indoor Air Quality of Offices in Six US Cities. *Building and Environment* **2013**, *60*, 243–253. https://doi.org/10.1016/j.buildenv.2012.10.013.

(14) Touchie, M. F.; Siegel, J. A. Residential HVAC Runtime from Smart Thermostats: Characterization, Comparison, and Impacts. *Indoor Air* **2018**, *28* (6), 905–915. https://doi.org/10.1111/ina.12496.

(15) Nguyen, J. L.; Schwartz, J.; Dockery, D. W. The Relationship between Indoor and Outdoor Temperature, Apparent Temperature, Relative Humidity, and Absolute Humidity. *Indoor Air* **2014**, *24* (1), 103–112. https://doi.org/10.1111/ina.12052.

(16) Nguyen, J. L.; Dockery, D. W. Daily Indoor-to-Outdoor Temperature and Humidity Relationships: A Sample across Seasons and Diverse Climatic Regions. *International Journal of Biometeorology; Heidelberg* **2016**, *60* (2), 221–229. http://dx.doi.org.ezproxy2.library.drexel.edu/10.1007/s00484-015-1019-5.

(17) Bertram, A. K.; Martin, S. T.; Hanna, S. J.; Smith, M. L.; Bodsworth, A.; Chen, Q.; Kuwata, M.; Liu, A.; You, Y.; Zorn, S. R. Predicting the Relative Humidities of Liquid-Liquid Phase Separation, Efflorescence, and Deliquescence of Mixed Particles of Ammonium Sulfate, Organic Material, and Water Using the Organic-to-Sulfate Mass Ratio of the Particle and the Oxygen-to-Carbon Elemental Ratio of the Organic Component. *Atmospheric Chemistry and Physics* **2011**, *11* (21), 10995–11006. https://doi.org/10.5194/acp-11-10995-2011.